STATIONARY AND MOVING SURFACE FFOWCS WILLIAMS AND HAWKINGS COMPUTATIONS OF AN ISOLATED RADIAL IMPELLER

Till HEINEMANN, Christoph SCHEIT, Matthias SPRINGER,
Stefan MÜLLER, Stefan BECKER

University Erlangen-Nuremberg, Inst. Process Machinery and Systems Engineering, Cauerstr. 4, 91054 Erlangen, Germany

SUMMARY

The program *SPySI* (Sound Propagation by Surface Integration) developed at the University of Erlangen uses an advanced time Ffowcs Williams and Hawkings algorithm. It is capable of integrating far-field sound emitted from a flow interacting with a solid body, on a stationary or moving porous surface wrapped around the source region. It is designed for turbomachinery applications with interfaces to input data generated with various flow simulation software. The Ffowcs Williams and Hawkings method is presented together with the *SPySI* algorithm. The correctness of the program is demonstrated with an analytical test case, and a short example of application is given.

INTRODUCTION

The incentive to compute aeroacoustic noise has been growing over the past years, as noise reduction has become more important. Consumer demand and legislative standards request more systematic and cost effective approaches in noise reduction. Computational methods are therefore increasingly attractive for industrial developers. This shifts the application of numerical aeroacoustics from classical aerospace applications towards turbomachinery.

This paper presents a post processing program for computational fluid dynamics (CFD) results that has an interface to various commercial and custom flow solvers and file formats. The program called *SPySI* is based on the porous Ffowcs Williams and Hawkings (FW-H) method. It was first introduced by Scheit et al. [1]. With flow data from a CFD computation on a surface wrapped around the aeroacoustic source region as input, the surface flow properties can be integrated to the acoustic signal perceived by observer points in the far field. Computational effort and precision are independent of

the observer's distance to the source region.

The code's modular structure grants flexibility for extension towards turbomachinery applications. *SPySI* bases on Farassat's Formulation 1, i.e. time differentiation is performed after surface integration [2]. An advanced time algorithm is used to find associated emission and observer times, as suggested by Brentner [3]. It has been pointed out that Farassat's Formulation 1A "could prevent some instabilities" [4], but since it requires more input data (time derivatives of the flow and surface geometry properties), its savings in computation are only relevant if these data are already exported by the CFD software. Because the program's objective is to minimize import demands or restrictions, Formulation 1 has been implemented.

The code can perform both stationary and moving surface flow simulations using two different modules, where the stationary mesh algorithm is less demanding towards memory usage. Still the rotating surface formulation bears the benefit that it can be chosen closer to the solid body surface inside a non-stationary domain. Although less quadrupole noise is covered this way, the results for low Mach numbers tend to be more precise due to the small quadrupole influence and the better CFD data resolution and exactness on the solid body boundary. Lyrintzis [4] gives an extensive comparison of different practical implementations of rotating and non-rotating surface formulations.

In the present state, the program is capable of computing the signal perceived by a stationary observer relative to an otherwise quiescent flow. Adaptions have been suggested by Casalino [5] to integrate a moving observer formulation or by Najafi-Yazdi [6] to superpose the flow with a uniform ambient flow rate, which is fit to resemble a wind tunnel situation. The projects *SPySI* was originally designed to be used in, all operate with Mach numbers $M < 1$. Therefore the mathematical Doppler singularity at $M = 1$ in the original FW-H formulation, has not yet been extended to cover transonic and supersonic source velocities. It is anyhow well possible and planned to do so in the future. Different possible adjustments to the FW-H algorithm are presented in [7] and [8].

NOMENCLATURE

$\hat{p}'$	analytical pressure signal
λ	wave length
ν	grid resolution
ρ'	acoustic density perturbation
σ	time resolution
τ	emission time
τ_i^e	element-specific emission time step
τ_{ij}	shear stress tensor
$\Box^2$	wave operator
c_0	speed of sound
f	surface function
g	retarded time function
L	numerical error
M_r	source Mach number towards observer
p'	acoustic pressure perturbation
r	distance source to observer
T	acoustic period
t	observer time
t_i^e	element-specific observer time step
T_{ij}	Lighthill stress tensor
u_i	fluid velocity
v_i	surface velocity
x_i	observer position
y_i	source position

THE FFOWCS WILLIAMS AND HAWKINGS METHOD

With the valid assumption of relatively small pressure and density fluctuations in comparison to the mean fluid properties, Lighthill [9, 10] derived his acoustic analogy

$$c_0^2 \Box^2 \left\{\rho'\right\} = \frac{\partial^2 \rho'}{\partial t^2} - c_0^2 \frac{\partial^2 \rho'}{\partial x_j \partial x_j} = \frac{\partial^2 T_{ij}}{\partial x_i \partial x_j} \tag{1}$$

with the Lighthill tensor T_{ij} comprising all source terms (excluding external forces), i.e. non-linear convective forces $\rho u_i u_i$, viscous forces τ_{ij}, and deviations in the speed of sound from c_0, $(p' - c_0^2 \rho')$,

$$T_{ij} = P_{ij} + \rho u_i u_j - \delta_{ij} \rho' = \rho u_i u_j - \tau_{ij} + \delta_{ij}(p' - c_0^2 \rho') \tag{2}$$

Equation (1) derives directly from the conservation of mass and momentum. It describes the origin and transport of aeroacoustic sound in a fluid in a second order linear hyperbolic partial differential equation (wave equation), with the wave operator $\Box^2 = \frac{1}{c_0}\frac{\partial^2}{\partial t^2} - \frac{\partial^2}{\partial x_i \partial x_i}$.
The (porous) Ffowcs-Williams and Hawkings method (FW-H) bases on an integral solution to eq. (1) [11]. It aims at replacing the immanent volumetric integral with a surface integral on $\mathscr{S}$, wrapped around the source region $\mathscr{V}$, defined by $f(x_i,t)$,

$$\begin{aligned} f(x_j,t) &< 0 \quad \text{if } x_j \text{ is located inside of } \mathscr{V} \\ f(x_j,t) &> 0 \quad \text{if } x_j \text{ is located outside of } \mathscr{V} \\ f(x_j,t) &= 0 \quad \text{if } x_j \text{ is located on } \mathscr{S} \end{aligned} \tag{3}$$

The multiplication of basic equations in the derivation of the Lighthill analogy with the Heaviside function $H(f)$, $H(f) = 1$ if $f \leq 0$ and $H(f) = 0$ if $f \geq 0$, with $\delta(x) = \frac{\partial}{\partial x} H(x)$, yields

$$\begin{aligned} \Box^2 \left\{ p' H(f) \right\} = & \frac{\partial^2}{\partial x_i \partial x_j} \left\{ T_{ij} H(f) \right\} \\ & + \frac{\partial}{\partial t} \left\{ \left[\rho \left(u_i - v_i \right) + \rho_0 v_i \right] n_i \left\| \frac{\partial}{\partial x_k} f \right\| \delta(f) \right\} \\ & - \frac{\partial}{\partial x_j} \left\{ \left[\rho u_j (u_i - v_i) + P_{ij} \right] n_i \left\| \frac{\partial}{\partial x_k} f \right\| \delta(f) \right\} \\ \doteq & q(x_j,t) \end{aligned} \tag{4}$$

using the linearized pressure density relation $p' = c_0^2 \rho'$. Here, u_i is the flow velocity while v_i represents the integration surface velocity. Equation (4) can be solved with the Green function given in eq. (5).

$$G(x_i,t;y_i,\tau) = \frac{\delta\left(t - \tau - \left\| x_i - y_i \right\| / c\right)}{4\pi \left\| x_i - y_i \right\|} = \frac{\delta\left(g\right)}{4\pi \left\| x_i - y_i \right\|} \tag{5}$$

It introduces the distinction of a signal's observer time and position t and x_i, and emission quantities τ and y_i, in the implicit time equation g.

$$g(x_i,t;y_i,\tau) = t - \tau - \frac{\left\| x_i(t) - y_i(\tau) \right\|}{c_0} = 0 \tag{6}$$

The condition $g = 0$ must be fulfilled for a valid signal. With the definition of two terms Q and L_j,

$$Q = \left(\rho \left(u_i - v_i \right) + \rho_0 v_i \right) n_i \,, \quad L_j = \left(\rho u_j (u_i - v_i) + p' \delta_{ij} - \tau_{ij} \right) n_i \tag{7}$$

the solution of eq. (4) is given by eq. (8), using co-moving coordinates $\eta_j = y_j - x_j^s(\eta_j,\tau)$. The remaining volume integral term has to be evaluated only outside of the defined source region $\mathscr{V}$. Consequently, it can be neglected if $\mathscr{V}$ is chosen sufficiently large around the acoustic sources.

$$\begin{aligned} 4\pi \left\{ p' H(f) \right\} (x_j,t) = & \frac{\partial^2}{\partial x_i \partial x_j} \int\limits_{\mathbb{R}^3} \left[\frac{T_{ij} H(f)}{r \left| M_r - 1 \right|} \right]_{\tau_e} \mathrm{d}^3 \eta_j \\ & + \frac{\partial}{\partial t} \int\limits_{\mathscr{S}} \left[\frac{Q}{r \left| M_r - 1 \right|} \right]_{\tau_e} \mathrm{d}\mathscr{S}(\eta_j) - \frac{\partial}{\partial x_j} \int\limits_{\mathscr{S}} \left[\frac{L_j}{r \left| M_r - 1 \right|} \right]_{\tau_e} \mathrm{d}\mathscr{S}(\eta_j) \end{aligned} \tag{8}$$

The last term in eq. (8) is usually referred to as "Loading-Noise". With the integration surface equal to the solid body surface, it represents the physical influence of the force of the solid body acting on the fluid. The other surface integral is denoted "Thickness Noise" and represents the physical mechanism of how strong the thrust on the fluid is that results from different surface element emission times due to the distance (i.e. thickness) discrepancies, in case of the integration surface collapsing with the physical solid body surface ("non-porous surface").

In eq. (8), τ_e implies the solution of the tagged term at the solution to g, r is the distance from source to observer $\|x_i - y_i\|$, and M_r is the source Mach number towards the observer,

$$M_r = r_j M_j = r_j \frac{v_j^s}{c_0} = \frac{r_j}{c_0}\frac{\mathrm{d}x_j^s}{\mathrm{d}\tau} = \frac{x_j - y_j}{c_0 \left\|x_j - y_j\right\|}\frac{\mathrm{d}x_j^s}{\mathrm{d}\tau} \tag{9}$$

Farassat's Formulation 1 (eq. (10)) reduces the amount of computations necessary for the evaluation of eq. (8) by transforming the divergence expression of L_j into a time derivative [2].

$$\begin{aligned} 4\pi \left\{p' H(f)\right\}(x_j,t) = {} & \frac{\partial^2}{\partial x_i \partial x_j} \int\limits_{\mathbb{R}^3} \left[\frac{T_{ij} H(f)}{r\,|M_r - 1|}\right]_{\tau_e} \mathrm{d}^3\eta_j \\ & + \frac{\partial}{\partial t} \int\limits_{\mathscr{S}} \left[\frac{Q\cdot c_0 + L_j r_j^n}{c_0\, r\,|M_r - 1|}\right]_{\tau_e} \mathrm{d}\mathscr{S}(\eta_j) + \int\limits_{\mathscr{S}} \left[\frac{L_j r_j^n}{r^2\,|M_r - 1|}\right]_{\tau_e} \mathrm{d}\mathscr{S}(\eta_j) \end{aligned} \tag{10}$$

This formulation is implemented inside the *SPySI* program code.

NUMERICAL METHOD, IMPLEMENTATION

In an algorithm for an integral method in aeroacoustics, the evaluation of a function $g = 0$ as in eq. (6), connecting source and observer time τ and t, is of high importance. Traditionally, there are two approaches for solving g. The retarded time approach evaluates equally spaced observer time steps t_i and iterates the various observer time steps τ_i^e for each element e as solutions to eq. (6). Computationally, this is not the most efficient algorithm for most cases [11], since the observer position $x_i(t)$ is usually fixed or can be described analytically, which often makes an analytical solution of g possible. The emission surface elements have more properties to update with time (surface normal, mid point, quadrature points etc.). Consequently, the advanced time approach considers the same equally spaced emission times τ_i for all surface elements, yielding custom t_i^e for each one of them. With the advanced time algorithm, the coordinate transformations of the grid properties can be performed as vector operations and only once for each (common) emission time step τ_i for all elements at the same time, and not nested inside a loop over all elements. This has advantages for parallelization of the algorithm too, since the surface can be easily subdivided [4]. t_i^e can be computed

$$t_i^e = \tau_i + \frac{\left\|x_j(t_i^e) - y_j^e(\tau_i)\right\|}{c_0} \tag{11}$$

which is an implicit function in general. Equation (11) though becomes explicit for fixed observers $x_i = const$, or can be rearranged into an explicit expression for simple motions.

SPySI reads information about the time row and possible surface mesh motion together with the flow data on it. The following steps are then carried out for each emission time step. The grid

element properties are updated according to the grid motion and the flow data. This includes node and quadrature point positions, normals, mid point velocities, and transformation coefficients. These arrays are multiplied with a rotation tensor, created from an angle ϑ and a rotation vector ρ_i,

$$R_{ij} = \delta_{ij}\cos\vartheta + \varepsilon^{ikj}\rho_k \sin\vartheta + (1-\cos\vartheta)\rho_i\rho_j \tag{12}$$

All element properties are pointed at inside array environments at grid level, such that vector operations can be used to update all properties, which are still accessible on element level. For the stationary version of the program, this step is of course omitted.

In a loop over all surface elements, distance r and projective source Mach number M_r are computed for the terms Q and L_j. The surface integrals in eq. (10) are evaluated with the selected quadrature scheme in computational space 2D coordinates (η, ζ)

$$I^{e,m}_{QL_r} = J^e \sum_i \sum_j w_i w_j \left.\frac{Q\cdot c_0 + L_j\, r^n_j}{c_0\, r\, |M_r - 1|}\right|_{\tau_m,(\eta_i,\zeta_j)} \tag{13}$$

$$I^{e,m}_{L_r} = J^e \sum_i \sum_j w_i w_j \left.\frac{L_j\, r^n_j}{r^2\, |M_r - 1|}\right|_{\tau_m,(\eta_i,\zeta_j)} \tag{14}$$

The two values $I^{e,m}_{QL_r}$ and $I^{e,m}_{L_r}$ are stored for each surface element at t^e_i. To generate a global acoustic signal, these must be differentiated or interpolated at common (observer) time steps $\hat{t}_j$. The interpolation of $I^{e,m}_{L_r}$ is performed with a piecewise Lagrangian polynomial using the n time step values closest to $\hat{t}_j$,

$$P^e_n(\hat{t}_k) = \sum_{i=0}^{n} I^{e,i}_{L_r} \prod_{\substack{j=0\\ j\neq i}}^{n} \frac{\hat{t}_k - t^e_j}{t^e_i - t^e_j} \tag{15}$$

and the differentiation of $I^{e,m}_{QL_r}$ is approximated with the derivative of $P^e_n(t)$ to t, i.e.

$$f'(\hat{t}_m) \approx \left.\frac{\mathrm{d}P_n(t)}{\mathrm{d}t}\right|_{\hat{t}_m} = \sum_{i=0}^{n} I^{e,i}_{QL_r} \sum_{\substack{j=0\\ j\neq i}}^{n} \frac{1}{t^e_i - t^e_j} \prod_{\substack{k=0\\ k\neq i\\ k\neq j}}^{n} \frac{\hat{t}_m - t^e_k}{t^e_i - t^e_k} \tag{16}$$

The results of eq. (15) and (16) are summed over all elements to produce the global acoustic pressure signal $p'(\hat{t}_i)$ of the entire surface mesh. In the stationary formulation of the algorithm, this is optimized in terms of memory usage by adding the element time steps' contribution to the global signal on the fly. Cyclic arrays store only so many time steps t^e_i, and because of the stationary nature of the geometry, the time steps t^e_i are always equally spaced, no matter their offset shift towards the global time steps $\hat{t}_i$. This means that the contribution of each element observer time to the global signal time steps in its proximity is known already before the next steps are computed, and the interpolation does not have to wait for these future t^e_i to be computed later. Extensive information on the *SPySI* program and all validation tests together with performance studies can be found in [12] and [13].

ANALYTIC TEST CASE

The correctness of the algorithm has been proven with an analytic test case. This consists of an acoustic monopole source located centrally inside a spherical surface grid with quadrangular elements. Two

test cases are presented, one with a stationary point source with the spherical mesh rotating concentrically around it, and one where both point source and mesh rotate eccentrically around the coordinate origin. The kinematics are illustrated in Figure 1 for the eccentric test case. For the validation of the FW-H code, the analytical pressure signal of the monopole is evaluated at a fixed observer position x_i with $\|x_i\| = 100$ as reference, while it is at the same time used to generate input data on the integration surface, as is the fluid velocity. They are

$$p'\left(x_j(t),t\right) = -\rho_0 \left\{ \frac{\partial \phi}{\partial t} + c_0 M_i^S \frac{\mathrm{d}\tau}{\mathrm{d}t} \frac{\partial \phi}{\partial x_i^S} \right\}, \quad u_i\left(x_j(t),t\right) = \left\{ \frac{\mathrm{d}}{\mathrm{d}x_i} \phi\left(x_j(t),t\right) \right\} \tag{17}$$

where the harmonic potential ϕ is a harmonic function in analogy to [15],

$$\phi(x_i,t) = \left. \frac{Q}{r(1-M_{r,S})} \right|_\tau, \quad Q(t) = \frac{A}{\rho_0 \omega} \exp\{i\omega t\} \tag{18}$$

It is evaluated at source emission time τ, again found by solving $g = 0$ as in eq. (6). The evaluation of the monopole source on the surface, with the mesh elements as observers, is performed with a retarded time algorithm. Different scenarios were examined. Besides different rotation velocities,

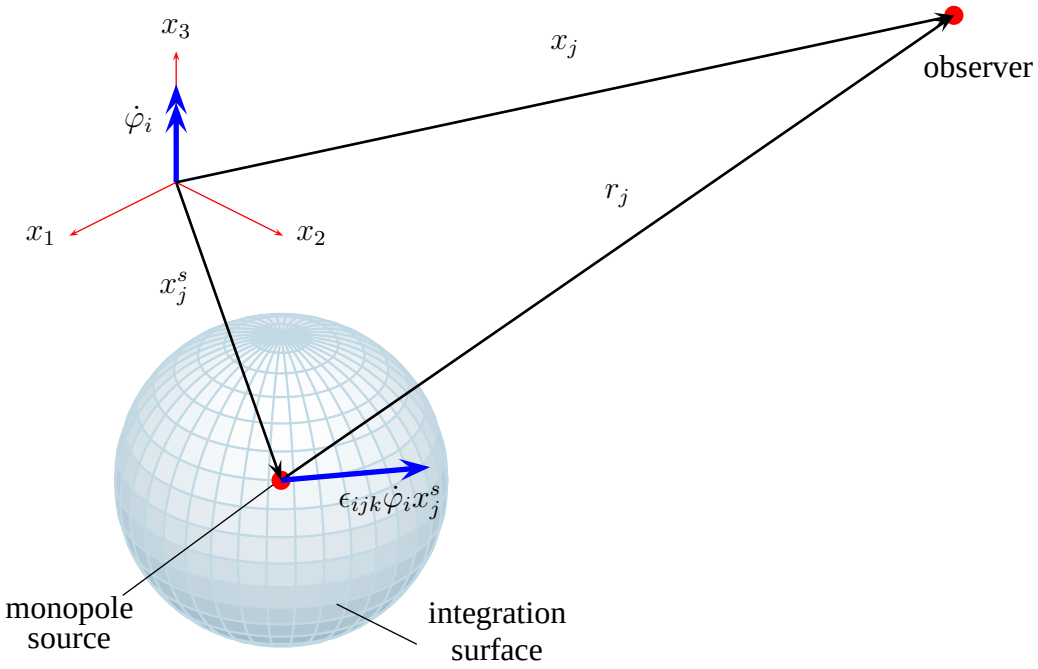

Figure 1: Eccentric rotation of one monopole source

leading to maximum surface Mach numbers $M_r \approx 0.67$, space and time resolution were varied. The time step resolution σ is simply the number of source time steps per acoustic cycle. Different amounts of elements on the same sized sphere, in combination with different source frequencies $\omega = f \cdot 2\pi$, yield different grid resolutions ν in relation to the monopole source wave length $\lambda = c_0/f$. It is

$$\sigma = \frac{T}{\Delta\tau} = \frac{1}{f\Delta\tau}, \quad \nu = \frac{\lambda}{\bar{d}_e} = \frac{f}{c_0}\sqrt{\frac{n_{el}}{4\pi r_{sphere}^2}} \tag{19}$$

In Figure 2, the FW-H pressure signals p' are plotted over t by way of example for a grid resolution of $\nu = 43.311$ and different time resolutions σ, together with the analytical reference signal $\hat{p}'$. It can

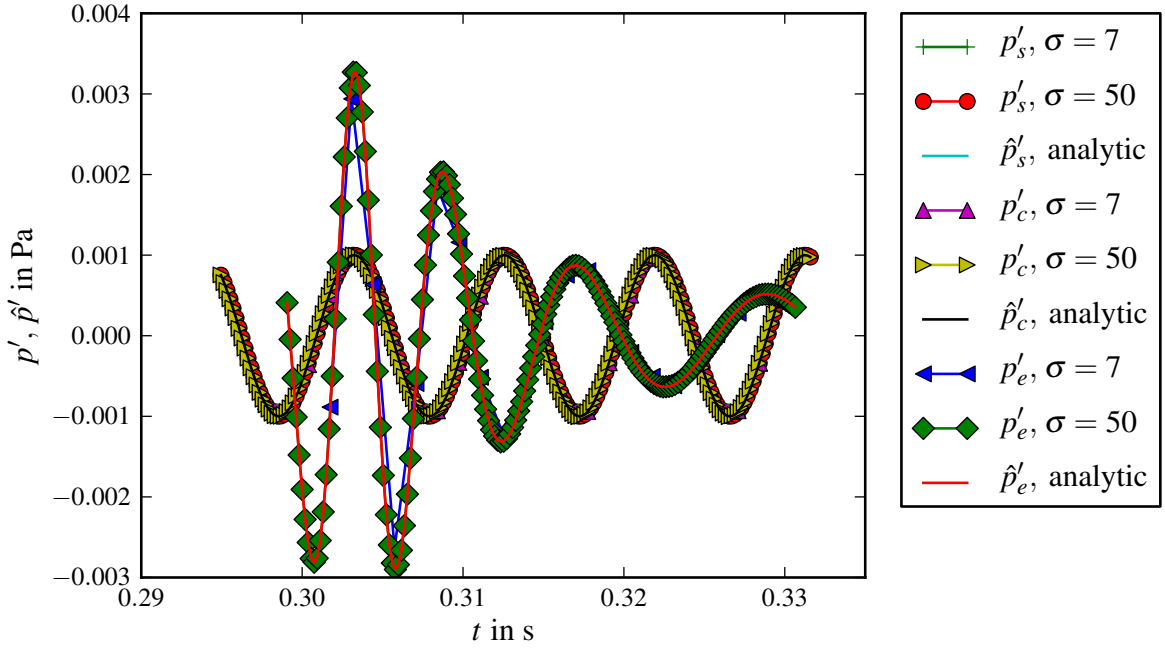

Figure 2: Analytical and FW-H integrated pressure signals over observer time

be seen that the static algorithm (index s) and the centric rotation (index c) produce the same pressure signal, while amplitude and frequencies of the eccentric case (index e) are shifted by the monopole source motion.

Since the exactness of the integral solution is difficult to tell from this mode of presentation, the scaled absolute error norm L is regarded. It is the root mean square deviation of the FW-H solution p' to the analytical solution $\hat{p}'$ over n time steps, scaled by the maximum analytical pressure,

$$L = \sqrt{\frac{1}{n}\sum_{j=1}^{n}\left(\frac{p'_j - \hat{p}'_j}{\sqrt{\max_i\left(\hat{p}'_i\right)^2}}\right)^2} \tag{20}$$

Figures 3 and 4 respectively show the L error plotted over the time and grid resolution σ and ν for static (s), centric (c) and eccentric (e) motion types with two different grid and time resolutions each. The figures indicate that the error behaves similarly for the different motion types. For the assessed resolution ranges, L varies between 0.2 for low resolution combinations and 4×10^{-4} for high resolution combinations. Both higher time and grid resolution result in significant improvements in the integral solution's exactness. The roughly linear data lines in the double log scale of the plot axes suggest a relation between L and the two resolutions with negative exponents. In both Figures 3 and 4 the slopes of the interpolated lines become greater in magnitude over the resolution on the abscissa if the other resolution variable is large. For Figure 3, this means for instance that the gradient over the data curve for $\nu = 161.03$ and eccentric motion, is greater in absolute value than for $\nu = 4.65$. Time and grid resolution appear to influence one another in their impact on the exactness of the FW-H solution.

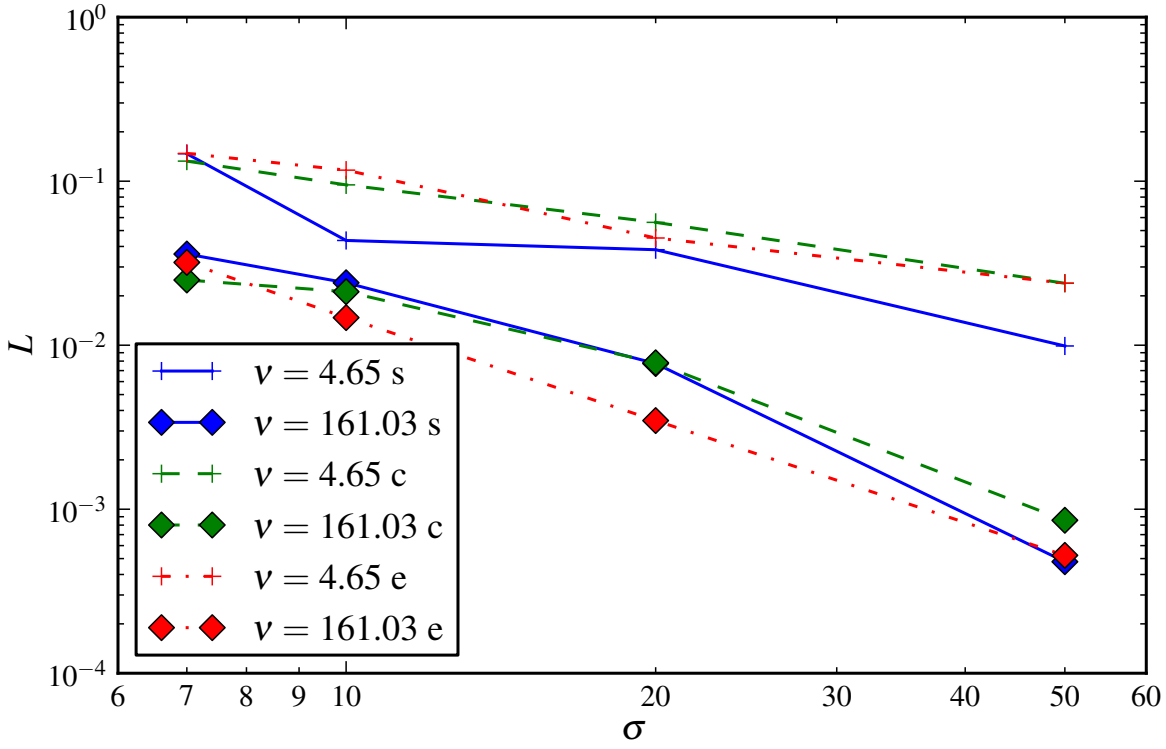

Figure 3: Absolute error L over time resolution σ

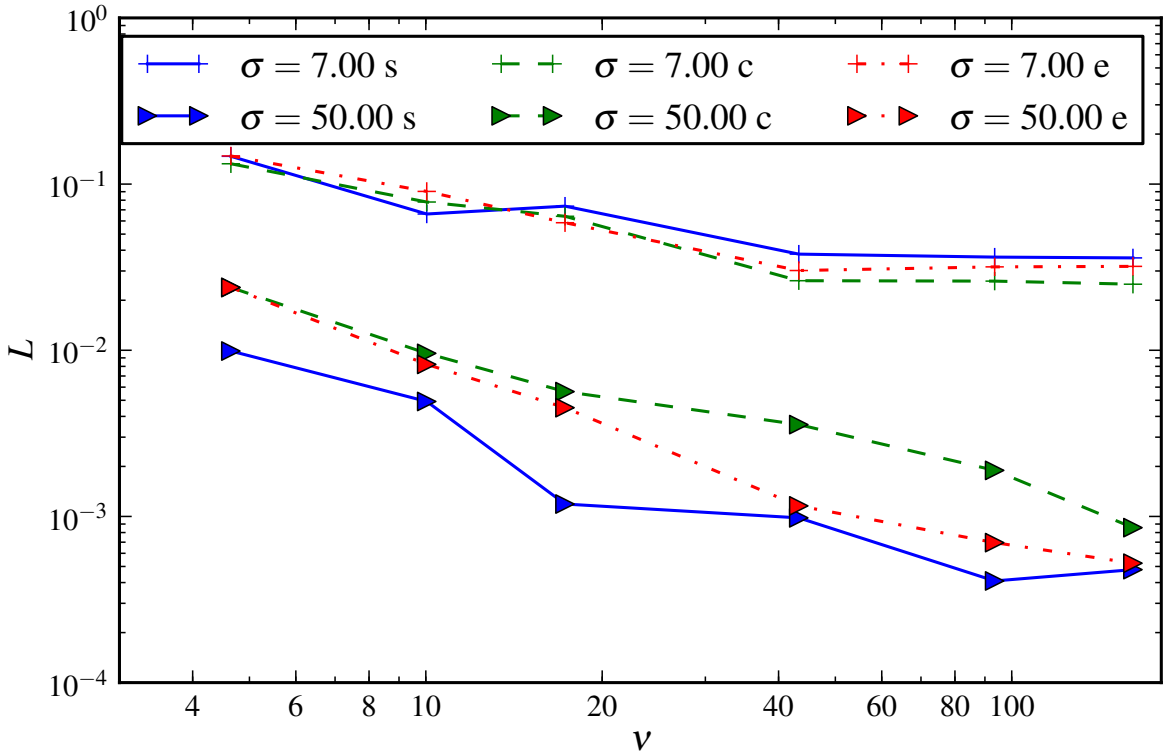

Figure 4: Absolute error L over grid resolution ν

COMPUTATION OF A RADIAL IMPELLER

To test the applicability of the *SPySI* code towards turbomachinery products, an isolated radial fan impeller was computed in a compressible URANS simulation (SST turbulence model) with ANSYS CFX13 to generate genuine CFD input data. The CFD domains are illustrated in Figure 5. One subdomain was defined to be rotating at $f = 2000$ rpm. It covers rotor and inlet cylinder. The walls of the cylindrical inlet (stator, marked yellow) counter-rotate in reference to the volumetric grid, to regain stationarity in space. There is a small inlet gap between rotor and stator with an opening boundary condition. The outlet area was covered by a second, stationary subdomain (marked green). Both subdomains were connected by a transient rotor stator interface at the physical outlet of the rotor. The complete grid consisted of a total of about 1.8 million volume elements. As boundary conditions, mass flow at the inlet of the stator (purple) and relative static pressure at the boundary of the outlet domain were used (all domain boundaries but the grid interface). A streamline plot of the CFD simulation results is shown in Figure 6, with transparent rotor and stator parts, and a pressure contour plot on the fan blades.
Since an isolated impeller is computed, mainly steady loading noise is to be expected, the interaction with the (inlet) rotor is not supposed to generate much noise. More sound sources may be created at the flow detachment at the trailing edges and in the turbulent outlet domain.

Two stationary surfaces were selected at the outlet of the ventilator for the FW-H algorithm. Around the impeller radius of 200 mm, two cylindrical integration surfaces were used to extract data from the CFD simulation every 5 CFD time steps, leading to an input time interval of 5×10^{-5} s over at total of 610 acoustic time steps τ_i.
The outlet surface had a distance of 10 mm to the outlet, while the more distant surface was positioned 50 mm away. Pressure, density and fluid velocity were integrated from there using eq. (10) towards a stationary observer located at $[1.0\,\text{m},\ 0.0\,\text{m},\ 0.0\,\text{m}]$. The pressure density spectra for both surfaces can be seen in Figure 7. The root mean square values of the noise emitted from the outlet surface was computed as 6.415 Pa or 110.124 dB. The distant surface lead to a root mean square value of 0.415 Pa, equivalent to 86.331 dB (no weighting filters applied). From Figure 7, it can be seen how the outlet surface noise is greater than the one integrated further away. This may be caused by more flow being covered by the cylindrical surface in closer proximity to the outlet (no top or bottom cover), as well as by the numerical dissipation of the higher frequencies which are not propagated well in the more coarse grid in the outflow region of the CFD simulation. This shows how important the choice of a good integration surface and exact input data are to the result of the FW-H computation. Nevertheless, the spectrum shows similar characteristic frequencies. Especially the first peak can be well explained. It is caused by one of the 10 blades passing by, rotating at about 33.3 Hz frequency, which results in a new blade passing every 3 ms.
The exclusion of volume integration of the quadrupole sources located outside of the integration surface in *SPySI* can be told from the following effect. Around 4 kHz, the distant surface signal may reflect noise created in the turbulent domain behind the fan exit. The sound created in this region is (partly) covered by the more distant surface, but it does not appear in the outlet surface signal.

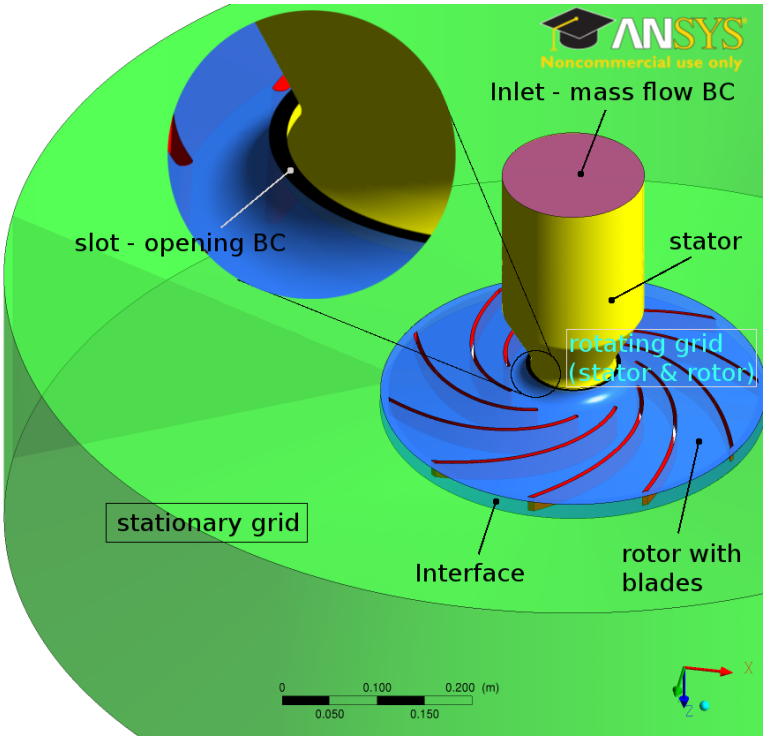

Figure 5: Domains and boundaries in the CFD computation

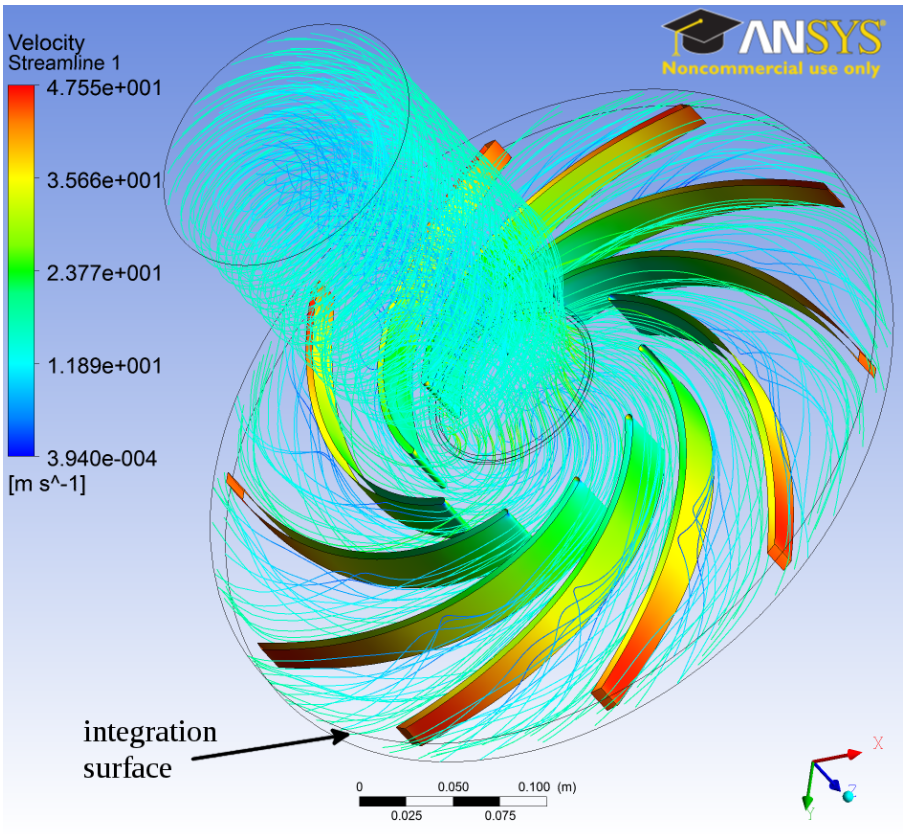

Figure 6: Streamlines in the CFD computation of the isolated radial impeller

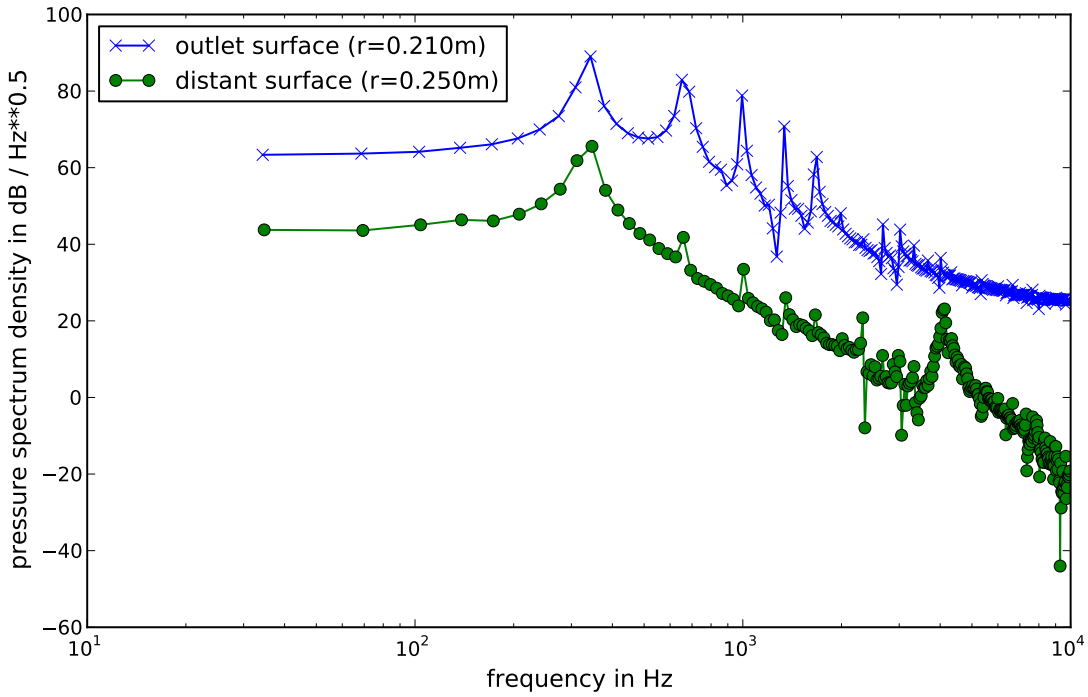

Figure 7: Pressure spectrum densities for two integration surfaces

CONCLUSION

It has been shown that an implementation of the FW-H algorithm for stationary and moving surfaces has been accomplished with good accordance to analytic test cases. The applicability to a technical example has been show for a radial ventilator computed with a URANS flow simulation. Surface data could be exported from ANSYS CFX13 and imported into the *SPySI* algorithm. The results showed realistic frequency spectra. Presently, a study of different integration surfaces in different distances to the solid body is being performed along with an assessment of the moving surface formulation for CFD input. The program itself is to be optimized more in its performance, i.e. parallelization of the code is aimed at along with the integration of C++ routines for heavy load routines inside the code. A moving observer formulation and an adaption to transonic motion are possible as well.

BIBLIOGRAPHY

[1] C. Scheit, B. Karic, A. Delgado, P. Epple, and S. Becker. *Experimental and Computational Study of Radial Impellers with respect to Efficiency and Noise Production*. In CMFF, editor, *Conference on Modelling Fluid Flow*. **2009**

[2] F. Farassat. *Derivation of Formulations 1 and 1A of Farassat*. Technical Report NASA/TM-2007-214853, NASA Langley Research Centre, **2007**

[3] K. Brentner. *A new Algorithm for Computing Acoustic Integrals*. Proceedings of the IMACS 14th World Congress on Computational and Applied Mathematics, **1994**

[4] A. Lyrintzis. *Surface integral methods in computational aeroacoustics – From the (CFD) near-field to the (Acoustic) far-field*. International Journal of Aeroacoustics, 2(2):95–128, **2003**

[5] D. Casalino. *An advanced time approach for acoustic analogy predictions*. Journal of Sound and Vibration, 261(4):583 – 612, **2003**

[6] A. Najafi-Yazdi, G. A. Brès, and L. Mongeau. *An acoustic analogy formulation for moving sources in uniformly moving media*. Proceedings of the Royal Society A: Mathematical, Physical and Engineering Science, 467(2125):144–165, **2011**

[7] K. S. Brentner. *Numerical Algorithms for Acoustic Integrals - the Devil is in the Details*. Technical Report AIAA 96-1706, NASA Langley Research Center, **1996**. Presented at 2nd AIAA/CEAS Aeroacoustics Conference (17th AIAA Aeroacoustics Conference)

[8] S. Loiodice. *Modelling Noise from Rotating Sources in Subsonic and Supersonic Regimes*. Ph.D. thesis, Cranfield University, School of Engineering, **2008**

[9] M. J. Lighthill. *On sound generated aerodynamically: I. General theory*. Proceedings of the Royal Society of London. Series A. Mathematical and Physical Sciences, 211:564–587, **1952**

[10] M. J. Lighthill. *On Sound Generated Aerodynamically. II. Turbulence as a Source of Sound*. Proceedings of the Royal Society of London. Series A. Mathematical and Physical Sciences, 222(1148):1–32, **1954**

[11] J. E. Ffowcs Williams and D. L. Hawkings. *Sound Generation by Turbulence and Surfaces in Arbitrary Motion*. Royal Society of London Philosophical Transactions Series A, 264:321–342, **1969**

[12] C. Scheit. *Implementation of a Ffowcs Williams and Hawkings (FW-H) method for aeroacoustic prediction*. Master of science thesis, University of Erlangen, **2007**

[13] T. Heinemann. *Implementation of a Ffowcs Williams and Hawkings (FW-H) formulation for moving surfaces*. Diploma thesis, University of Erlangen, **2011**